Acta Materialia 186 (2020) 162–171

Contents lists available at ScienceDirect

Acta Materialia

journal homepage: www.elsevier.com/locate/actamat

Full length article

Comparative study of radiation defects in ion irradiated bulk and thin-foil tungsten

Ruo-Yao Zheng, Wei-Zhong Han*

Center for Advancing Materials Performance from the Nanoscale, State Key Laboratory for Mechanical Behavior of Materials, Xi'an Jiaotong University, Xi'an 710049, China

ARTICLE INFO

Article History:
Received 27 August 2019
Revised 23 December 2019
Accepted 27 December 2019
Available online 6 January 2020

Keywords:
Tungsten
Irradiation
Dislocation loops
Helium bubbles
Cavities

ABSTRACT

In this study, we employ transmission electron microscope (TEM) to analyze radiation defects in helium (He) and krypton (Kr) ions implanted bulk and thin-foil tungsten. For bulk tungsten, subgrains are formed near the surface region under both He^+ and Kr^+ irradiation. Dislocation loops are observed beyond ion implanted range. These observations are related to self-interstitial atoms (SIAs) diffusion and clustering. Ordered bubbles are formed in He^+ implantation, while no cavities are detected in Kr^+ irradiation. In thin-foil tungsten, line up of dislocation loops is found mainly aligns along {101} and {112} slip planes. Both 1/2<111> and ⟨100⟩ dislocation loops are identified. Compared to He^+ irradiation, more ⟨100⟩ loops are detected in Kr^+ irradiation due to higher energy collision cascade. Nanocavities are detected in irradiated thin-foil tungsten besides the formation of high density of interstitial loops. The number density of dislocation loops and the volume fractions of cavities are higher in He^+ irradiation than in Kr^+ irradiation. The differences in nature of radiation defects is attributed to the higher recombination rate of vacancies and interstitials in bulk sample, the significant surface sink effect in thin-foil irradiation and the chemical and physical effect of implanted ions.

1. Introduction

Tungsten is one of the promising plasma-facing materials for future fusion reactors because of their high melting point, high thermal conductivity, low tritium retention and excellent sputtering erosion resistance etc. [1]. During service in fusion reactor, tungsten experiences high heat fluxes, high energy helium (He) ions bombardment and fast neutrons irradiation damage [2,3]. Both ion and neutron irradiation induce high density of defects, for example, dislocation loops, He bubbles etc. [4–9]. Radiation defects have a marked impact on the thermal conductivity [10], mechanical properties [11,12], and tritium retention behaviors of tungsten [13,14]. Therefore, the character of radiation defects and their effect on thermal and mechanical properties of tungsten are of practical interest and thus widely investigated in past decade.

The character of radiation defects formed in tungsten were explored under neutron, heavy ion and He ion irradiation. Voids were the major damage structures in pure W after neutron irradiation at elevated temperature [15–20]. Dislocation loops were also observed under lower dpa levels but their number density was 1–2 orders of magnitude less than that of the voids [15–20]. Faceted cavities were formed in both single and polycrystalline tungsten after neutron irradiation at high temperature [15–20]. The distribution of cavities was affected by the sink effect of grain boundaries (GBs) and this phenomenon is identical to the irradiated Cu [21].

Defects in self-ion irradiated tungsten were carefully examined at temperature ranging from 300 to 750 °C [22,23]. Interstitial dislocation loops with 1/2<111> Burgers vector were observed in most cases. The diameter of loops was less than 20 nm and had a peak distribution around 6 nm. The number density of dislocation loop was about 10^{22} to 10^{23} m^{-3}. With increasing the irradiation temperature, the size of dislocation loop increases while their number density decreases [22,23]. Under self-ion bulk implantation, higher density of dislocations was observed near the surface region. Subsequent annealing induced significant growth of dislocation loops. Most of dislocation loops were perfect dislocations with the Burgers vectors of b = 1/2<111> [24]. Both dislocation loops with the Burgers vector of 1/2<111> and ⟨100⟩ loops were observed in tungsten under 3 MeV Cu^+ irradiation at room temperature [25]. Nanocrystalline tungsten had lower loop damage and less void swelling than their coarse grained counterpart [25–27].

Dislocation loops with Burgers vector of 1/2<111> were also observed at irradiation temperatures of 500 °C and 750 °C, and no loops were observed at 1000 °C under He^+ implantation [28,29]. Both vacancy and interstitial loops were detected. He bubbles were observed for all He/DPA ratios, and the size of bubbles increases and their number density decreases with raising irradiation temperature. Under dual

* Corresponding author.
E-mail address: wzhanxjtu@mail.xjtu.edu.cn (W.-Z. Han).

https://doi.org/10.1016/j.actamat.2019.12.053
1359-6454/

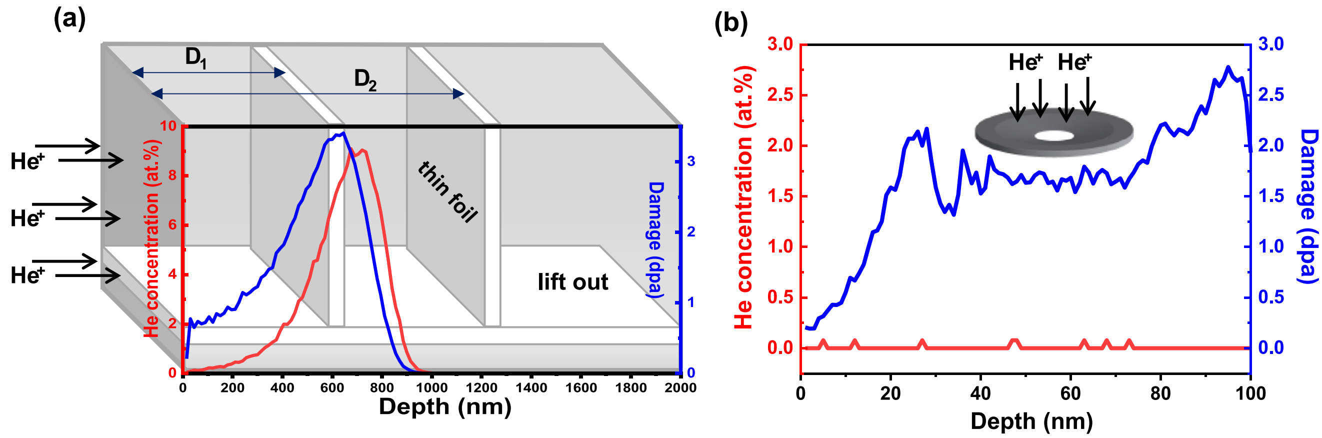

Fig. 1. Schematic illustration of He implantation in bulk samples and TEM foils. He ion beam was tuned to implant near perpendicular (7°-off) to the surface of TEM foils and the top surface of bulk samples. (a) Bulk implantation and corresponding He concentration (red line) and damage distribution (blue line) predicted by SRIM. Vertical slices represent thin TEM foils cut at different depths, where the radiation depth D means the sample is cut from a depth of D to D ± 25 nm. Horizontal slice represents lift out cross-section sample to study the defects distribution across the whole range. (b) He concentration (red line) and damage distribution (blue line) in TEM foil were calculated by SRIM.

beam irradiation (Fe^{3+} and He^+) [30], profuse dislocation loops were observed in the sub-surface region and at the end of the damaged area. Both dislocation lines and loops were observed in all irradiation temperatures, while bubbles were formed only above 500 °C.

Up to date, the analyses of radiation defects in tungsten were mainly performed with transmission electron microscope (TEM) thin-foil irradiation in which a strong surface effect cannot be neglected [22,31]. Although there are some samples were irradiated in bulk tungsten and then characterized in a form of TEM foil after irradiation [9,23,32], only radiation defect at fixed depth can be captured. Overall, the experiments described above have less investigations on the defects distribution along radiation depths [24,30], and no comparative study to reveal the influence of surface sink effect on radiation defects dynamics. Actually, the nature and distribution of radiation defects in bulk tungsten and their dynamics is closer to the real service condition in fusion nuclear reactor. In addition, the difference of defect structures in bulk and thin-foil tungsten is important for us to judge the validity of thin-foil irradiation experiment. In order to fully understand the character of radiation defects in tungsten, the distribution of defects at various implantation depth and their comparison with thin-foil irradiation should be addressed. Besides, the chemical and physical effect of light and heavy ions are also needed to be explored under a similar irradiation condition.

In this study, we characterize the irradiation defects in both bulk and thin-foil tungsten irradiated with He or Krypton (Kr) ions at the same temperature (400 °C). Radiation microstructures were analyzed by diffraction contrast techniques in TEM. Defects distribution, configurations, sizes, number density and their nature were investigated in details. The difference in character of irradiation defects in bulk and thin-foil irradiation were discussed based on the recombination rate of vacancies and interstitials, the surface sink effect in thin-foil irradiation and the chemical and physical effect of implanted light and heavy ions.

2. Experimental methods

High-purity tungsten (>99.95%) were used in this study. Both bulk disk and thin-foil samples were used in ion implantation. The bulk samples were prepared by cut, ground and polishing and have a final thickness of 40 μm. The thin-foils were first ground to 40 μm, then these samples were dimpled by an M200 Dimpling Grinder, and further thinned to less than 50 nm using an Ar^+ ion milling on an M1050 TEM Mill, operated with the final voltage of 3 kV and beam angle of 4°.

He^+ implantation was performed on the bulk samples with energy of 400 keV using a NEC 400 kV implanter. The implantation lasted for 200 min and the ion fluence is 2×10^{17} ions/cm^2 (corresponding to a dpa rate of 2.83×10^{-4} dpa/s). The thin-foil samples were implanted to a fluence of 5×10^{17} ions/cm^2 in order to achieve a similar damage level as the bulk sample at 400 °C (lasted for 240 min and with a dpa rate of 1.94×10^{-4} dpa/s). Kr ion irradiation was performed using a NEC implanter as well, with ion energy of 800 keV at 400 °C. Both bulk and thin-foil samples were irradiated with a dpa rate of 0.02 dpa/s and lasted for 18 min with total influence of 5×10^{15} ions/cm^2. The ion beam was tuned 7° off compared to the normal of samples in order to avoid channeling effect. The irradiation damage and the He^+/Kr^+ concentration as a function of depth from the top surface can be calculated by the Stopping and Range of Ions in Matter (SRIM) [33] with threshold displacement energy of 90 eV [34] and lattice binding energy of 0 eV [35] for tungsten. Fig. 1 shows the variation of dpa (blue line) and He concentration (red line) with implantation depth in both bulk and thin-foil tungsten.

In order to study the character of irradiation defects at different depth, cross-section TEM samples, oriented parallel to the implantation direction, were lifted out using a focused ion beam (FIB) manipulator (Helios 600) on the bulk tungsten, as shown in Fig. 1a. During FIB preparation, the top surface was protected by Pt layer. TEM sample with size of 10 $\mu m \times 8$ $\mu m \times 2$ μm was lifted out from the bulk tungsten. It was further thinned to about 50 nm and cleaned with final Ga^+ beam with energy of 5 kV and current of 46 pA. Different thin foil samples were cut at a selected implantation depth of D. D was defined as the depth from the top surface of the implantation. The ion beam current was reduced to 1.5 pA with 30 kV Ga^+ for the final thinning, and the flashing electrolytic polishing was performed in the solution 0.5 wt% NaOH aqueous at a voltage of 15 V about 0 °C to remove the FIB-induced surface damage. The thicknesses of the thin-foil samples is around 200 nm before flashing polishing, and has a final thickness of 50 nm. Hence the sample at a depth D means that it spans from D-25 to *D* + 25 nm. At least two thin-foil were cut for defects characterization at each depth. Two-beam diffraction contrast as well as defocus imaging were used to study the radiation defects using a JEOL 2100F TEM. All He bubbles were observed with a defocus of −1500 nm.

3. Results

3.1. Radiation defects in helium implanted bulk tungsten

According to the SRIM simulation in Fig. 1a, the range of He concentration and damage is about 1 μm, thus the irradiation defects at various depths should be different. Fig. 2a shows the character of defects in the whole range of He implanted bulk tungsten. In the range of 0 nm to 400 nm, some sub-micron grains and several GBs

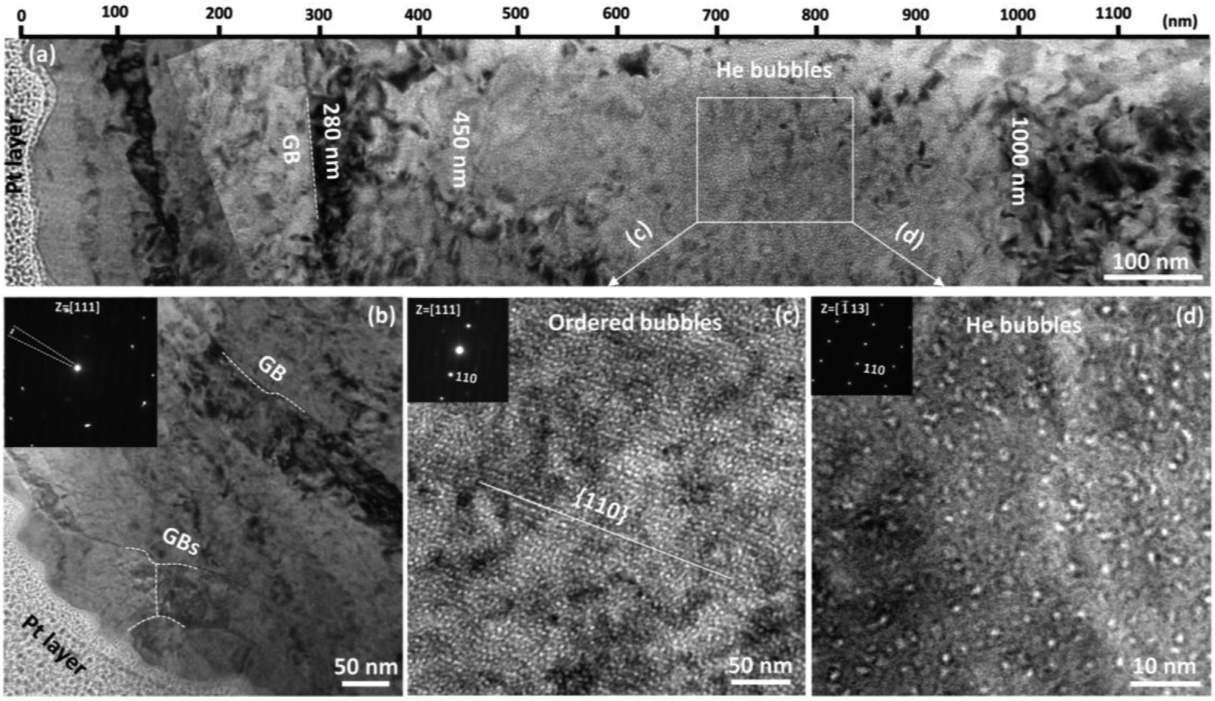

Fig. 2. Cross-section TEM to show the distribution of defects across the whole range of He implanted tungsten. The implanted surface was covered with a protective Pt layer. (a) The overall view of He irradiated tungsten. (b) Sub-micron grains formed in the top 300 nm range of He implanted tungsten. The tiny misorientation angle of grain boundaries is indicated by the split of the diffraction spot. (c) Ordered He bubbles formed at the peak He concentration region. (d) He bubbles with the diameter of 1.5 nm formed between D = 450 and 1000 nm.

are formed. Fig. 2b displays the details of these irradiation induced GBs. The GBs has misorientation angle less than 5°, as indicated by the elongated diffraction spots in Fig. 2b. The sub-micron grains are more or less elongated and near parallel to the implanted surface. Numerous He bubbles are observed in the range of 400 nm to 1000 nm, and reaches a peak around 700 nm, which is consistent with the peak He concentration region in Fig. 1a. Fig. 2c and d highlight the morphology of He bubbles. At peak He concentration region (D = 700 nm), ordered He bubbles are aligned along the (110) plane when viewed along ⟨111⟩ direction (Fig. 2c). Fig. 2d shows the enlarged He bubbles in the peak He concentration region with electron beam close to [113]. The average He bubbles diameter is about 1.5 nm, and the size of He bubbles is independent of He concentration. He bubbles are not perfect spherical and lost the ordered character under viewing directions other than ⟨111⟩.

The characters of dislocation loops were studied by cutting thin-foil at different depth, as illustrated in Fig. 1a. Fig. 3 shows the dislocation loops formed at various depths. All images were taken under a two-beam diffraction contrast condition with zone axis of [111]. Fig. 3a presents a typical image of dislocation loops formed at D = 200 nm. At this depth, the damage and He concentration are 0.9 dpa and 0.4 at.%, respectively. Only isolated dislocation loops were identified in this region in addition to some dislocation lines. The loops number density is increased slightly at D = 300 nm (with 1.2 dpa and 0.8 at.% He), as shown in Fig. 3b. At D = 500 nm (2.6 dpa and 3.7 at.%), more dislocation loops were observed (Fig. 3c). At D = 700 nm (2.8 dpa and 8.8 at.% He), the density of dislocation loops decreases slightly (Fig. 3d). At D = 900 nm, although the irradiation damage and He concentration decrease to 0.06 dpa and 1.0 at.%, the loop number density is increased to a peak value within all range of the implanted region, as shown in Fig. 3e. Dislocation loops are also identified at the region beyond the He implantation with 0 dpa and He concentration at D = 1100 nm, as displayed in Fig. 3f. To a deeper region with D = 1700 nm, no dislocation loops were found (Fig. 3g). The variation of the number density and the size of dislocation loop are plotted in Fig. 3h. The diameter and number density of dislocation loops have a weak correlation with damage level (blue dotted line) and He concentration (gray dotted line), as shown in Fig. 3h. The minimum loops density (2.4×10^{21} /m^3) appears at D = 200 nm. Then loops number density reaches a plateau between D = 300 nm and 700 nm. Once beyond the peak He concentration region, the dislocation loop number density reaches a peak value of 4.0×10^{22} /m^3 at D = 900 nm. Beyond the He implanted range, the loops density drops to 6.3×10^{21} /m^3 at D = 1100 nm and to zero at D = 1700 nm. The diameters of dislocation loops remain constant around 4 nm, which is independent of radiation damage and He concentration as well.

3.2. Radiation defects in helium implanted thin-foil tungsten

Compared with radiation in bulk tungsten, due to lack of recoil atoms, the average radiation damage in TEM foils is about 1.8 dpa and the He concentration is 0.1 at.%, as shown in Fig. 1b. Fig. 4 shows the typical radiation defects formed in TEM foil tungsten after He implantation. All images were taken under a two-beam diffraction contrast condition. A large number of dislocation loops can be observed under z=[111] in Fig. 4a. Dislocation loops clusters are forming spatial ordering, mainly distributed along {110} and {112} planes when viewed along ⟨111⟩ direction, as marked in the enlarged images in Fig. 4b and c. However, the dislocation loops clusters is not obvious when viewed along z=[011], and only a small fraction of loops show contrast, as shown in Fig. 4d. Under viewing direction of z=[001], individual dislocation loop can be identified (Fig. 4e). In addition to dislocation loops, abundant radiation-induced cavities with average diameter of 1.3 nm are also formed in TEM foil tungsten, as displayed in Fig. 4f.

Fig. 5 displays the method to determine the Burgers vector of dislocation loops under four different vectors with z=[001]. All the dislocation loops used for Burgers vector examination are in the same regions. The dislocation loops in red squares in Fig. 5a, c and d are visible under $g = \bar{1}10, \bar{2}00$ and 020, and they are invisible under g = 110, as shown in Fig. 5b. More details can be observed in Fig. 5e, g, i and k, which are the enlarged images of the red squares in Fig. 5a, b,

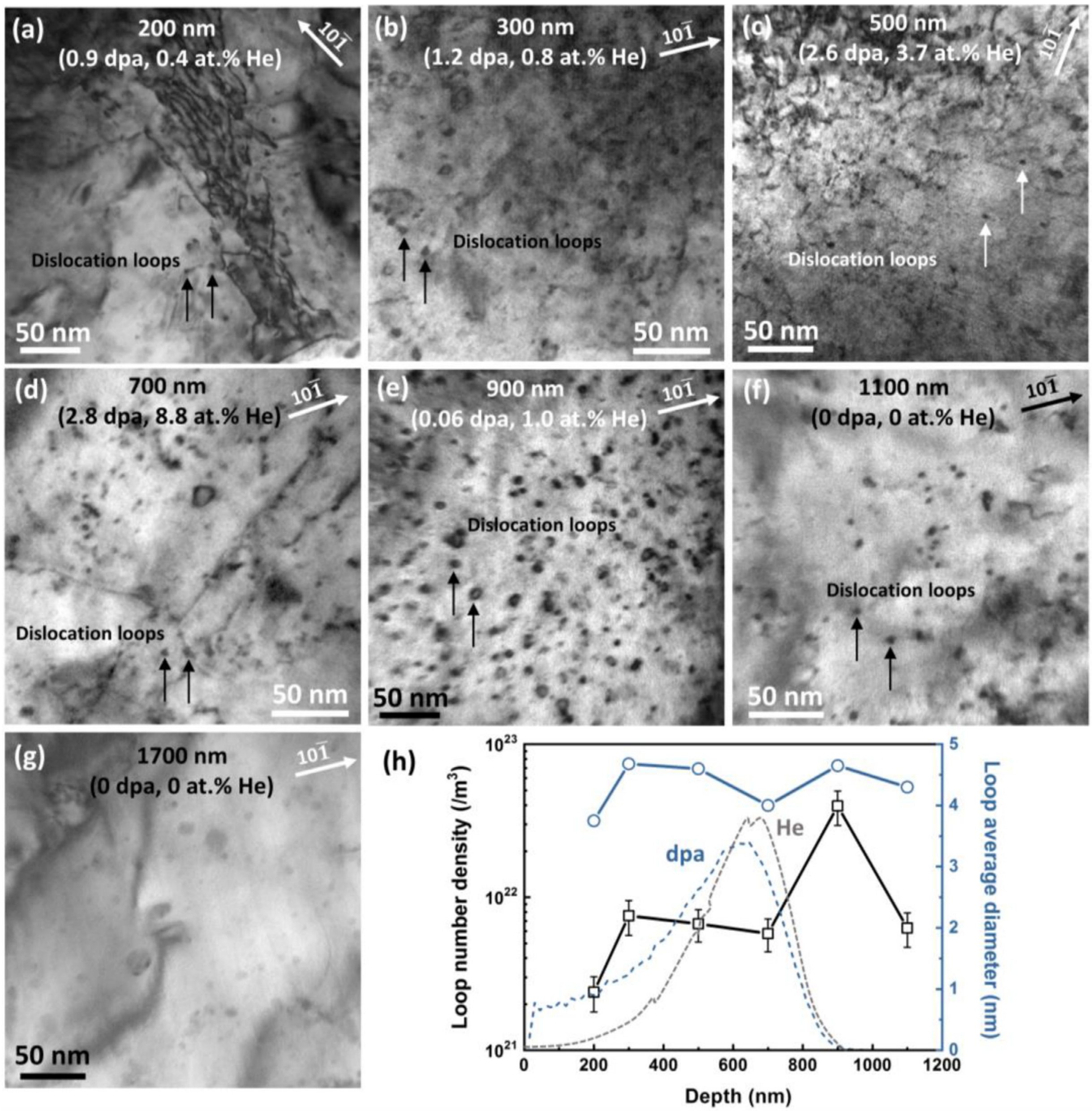

Fig. 3. Distribution of radiation-induced dislocation structures at different depths in He irradiated bulk tungsten. All samples were cut by FIB and then cleaned by flash polishing. Typical image of dislocation loops formed at depths of (a) D = 200 nm, (b) D = 300 nm, (c) D = 500 nm, (d) D = 700 nm, (e) D = 900 nm, (f) D = 1100 nm and (g) D = 1700 nm. Some dislocation loops are labeled by arrows. (h) Variations of dislocation loop density (black line) and loop diameter (dark blue line) with depths in He implanted bulk tungsten. (For interpretation of the references to colour in this figure legend, the reader is referred to the web version of this article.)

c and d. The solid and dashed lines represent their visibility and invisibility. According to the invisibility criterion, the Burgers vector of dislocation loops in red squares is 1/2<111>. While the dislocation loops in yellow squares have contrast under $g = \bar{1}10$, 110 and $\bar{2}00$, as shown in Fig. 5a, b and c. All these dislocation loops lost contrast under g = 020 (Fig. 5d), indicating that these are ⟨100⟩ dislocation loops. Similarly, enlarged dislocation loops are highlighted in Fig. 5f, h, j and l. Two types of dislocation loops were identified in He implanted tungsten, and their size and number density were measured and summarized in Fig. 8.

3.3. Radiation defects in krypton irradiated bulk and thin-foil tungsten

The character of radiation defects in Kr^+ implanted bulk tungsten were also studied, as shown in Fig. 6. The peak Kr concentration is about 0.47at.% (red line, at D = 125 nm) and the peak damage is about 21 dpa (blue line, at D = 75 nm) according to the SRIM simulation, as marked in Fig. 6a. In the 300 nm range of Kr^+ irradiated area, several sub-micron grains and curved GBs were formed. Fig. 6b highlights the details of the sub-micron grains and GBs formed after Kr^+ irradiation. According to the inserted diffraction pattern in Fig. 6a, these GBs have a misorientation around 10°. No sub-micron grains can be detected beyond the Kr^+ irradiated region. Similarly to the He^+ irradiated bulk tungsten, the sub-micron grains are also elongated and near parallel to the implanted surface. However, these sub-micron grains have higher misorientation than GBs formed in He^+ implantation. In addition, no cavities can be identified in the whole range of Kr^+ implanted bulk tungsten except some dislocation loops.

In the Kr^+ irradiated thin-foil tungsten, the peak Kr^+ concentration is 0.4 at.% and the irradiation damage is about 21.5 dpa. Fig. 7 shows the typical irradiation defects formed in TEM foils after Kr^+ implantation. All images were taken under a two-beam diffraction contrast

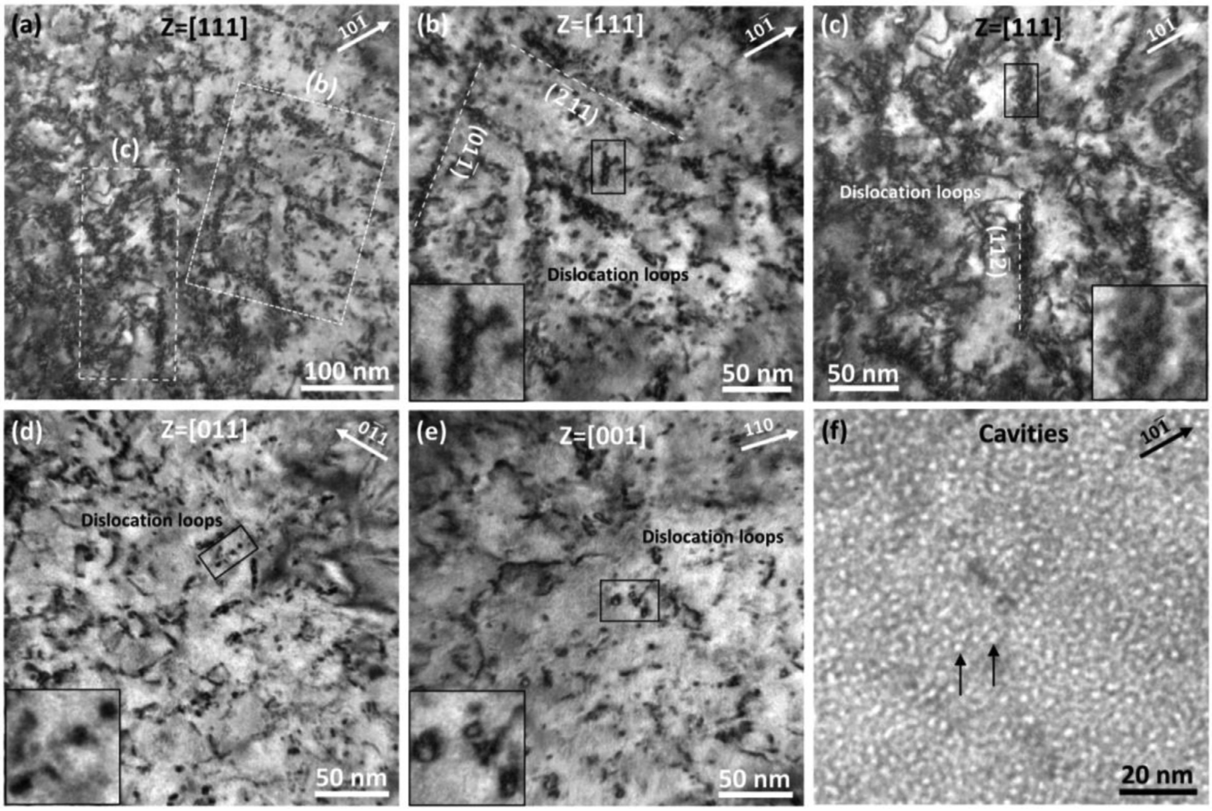

Fig. 4. Defects structures in He irradiated TEM foil tungsten. (a) High density of dislocation loops formed in TEM foil tungsten. (b) and (c) are the enlarged images of the rectangles in (a). (b) Highlight the distribution of dislocation loops along specific crystalline planes. (c) Dislocation striations formed in He irradiated tungsten TEM foil with electron beam along *z*=[111]. (d) Dislocation structures observed along *z*=[011], (e) Dislocation structures viewed along *z*=[001]. (f) High density of voids formed in He irradiated TEM foil tungsten.

condition with zone axis close to [111], [011] or [001]. Similar to He^+ irradiation, a large number of dislocation loops can be identified under *z*=[111], as shown in Fig. 7a. Dislocation loop clusters also show clear spatial ordering, mainly lining-up along {101} and {112} planes. However, the dislocation loops clusters are not obvious when viewed along *z*=[011], as demonstrated in Fig. 7b. Under viewing direction of *z*=[001], individual dislocation loop can be identified in Fig. 7c. Using similar method in Fig. 5 and the invisibility criterion g·*b* = 0, the Burgers vector of dislocation loops in Kr^+ irradiated TEM foils were also determined. Both 1/2<111> and ⟨100⟩ loops can be identified. High density of cavities with average size of 1.2 nm were also formed under Kr^+ thin-foil irradiation, as shown in Fig. 7d. The size and density of dislocation loops and the volume fraction of cavities are summarized in Fig. 8.

4. Discussion

4.1. Comparison of helium irradiated bulk and thin-foil tungsten

In order to assess the effect of He on defect development, detailed characterization of irradiation defects across the whole range of implanted region in both bulk (Figs. 2 and 3) and thin-foil tungsten (Fig. 4) were performed. Bulk tungsten irradiation provides an opportunity to witness the defects character and their evolution at various dpa and He concentration. In the range of 0 to 300 nm, sub-micron grains and low angle GBs are formed in the sub-surface region. Ultrafine grains were reported to form in ceramic due to He-induced surface blistering [36]. However, the formation of blister cannot happen in current implantation because of the low irradiation temperature (~0.12 T_m). The sub-micron grains and low angle GBs are likely a product of the accumulation of irradiation induced point defects. In tungsten, the migration energy of self-interstitial atom (SIA) ($E_i^m = 0.08$eV)[7] is more than one order of magnitude lower than the migration energy of vacancies ($E_v^m = 1.7$eV)[9]. During irradiation at 400 °C, tungsten SIAs have much higher mobility and tend to accumulate at the sub-surface due to the sink effect of top surface. Exceptional high concentration of SIAs can develop into high density of dislocations and their aggregation further evolve into sub-micron grains separated by low angle GBs [37]. The formation processes of ultrafine-grain due to the accumulation of dislocations have been widely evidenced in severe plastic deformation of metals [38,39]. Abundant point defects are produced during irradiation [40]. Migration, clustering of point defects and their further evolving into sub-microns grains are an important route to mitigate the dilatational stress induced by SIAs. Due to the lower He concentration, He bubbles are scarce in the subsurface regime (Fig. 2a).

With the increase of He concentration and irradiation damage in the range from *D* = 300 nm to *D* = 900 nm, high density of He bubbles is formed. In general, the He interstitials have low migration energy while the substitutional He is easily trapped at vacancies because of their high binding energy [41]. As a result, a large number of He atoms are trapped by vacancies and form into stable He-vacancy (He-V) clusters. The He−V clusters have high binding energy with other point defects as well, and thus can as sinks to further capture other He interstitials and vacancies or even smaller He clusters, which give rise to He bubble nucleation and growth [42–45]. As a results, high density of nanoscale He bubbles are formed in this region in addition to interstitial type of dislocation loops (Figs. 2c and 3d).

As shown in Fig. 3, the maximum loop number density appeared at the depth of *D* = 900 nm, although the irradiation damage is only 0.06 dpa, which is beyond the peak He concentration and maximum irradiation damage regime. The formation of high density of dislocation loops are related to the inward diffusion of SIAs at 400 °C. According to Fig. 1a, the radiation damage and He concentration is

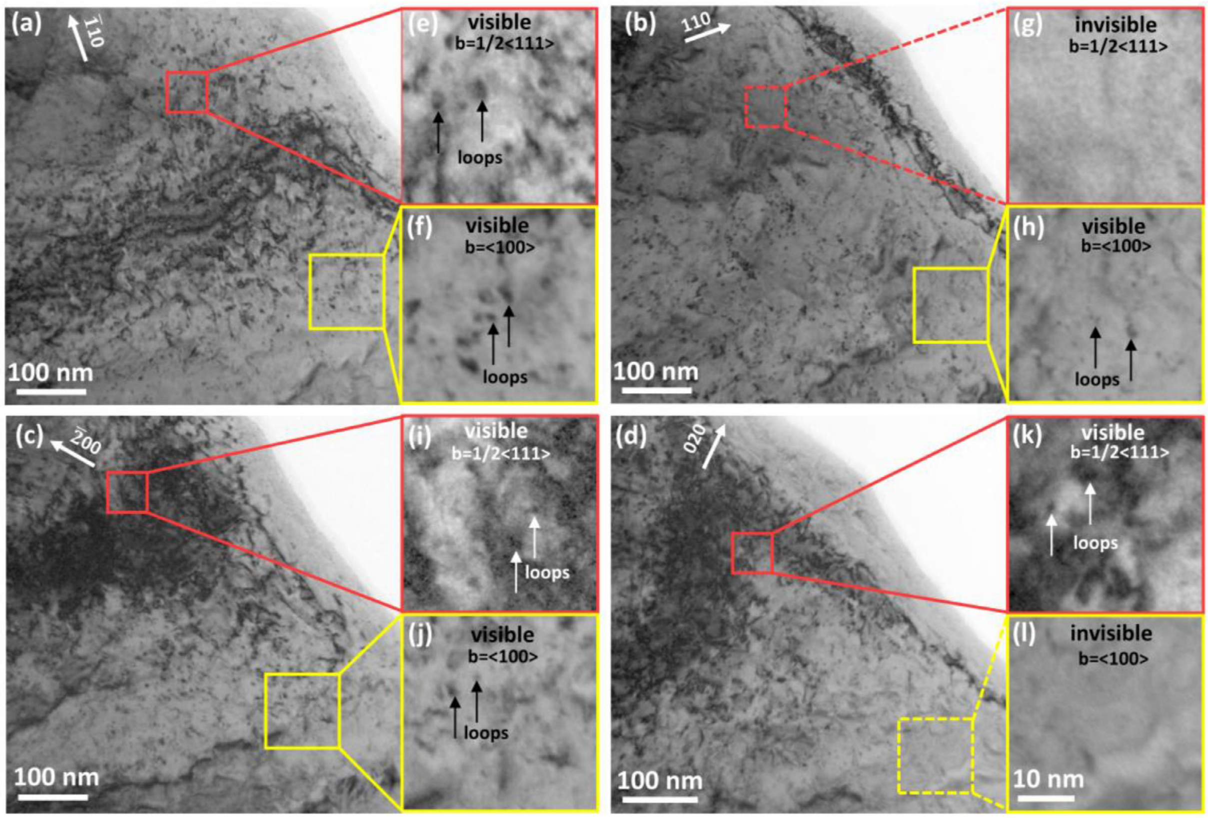

Fig. 5. Determination of Burgers vector of dislocation loops in He irradiated TEM foil tungsten. Images are taken under z= [001] with four g vectors of (a) [$\bar{1}$10], (b) [110], (c) [$\bar{2}$00] and (d) [020]. (e) and (f), (g) and (h), (i) and (j), (k) and (l) are enlarged TEM images in the region marked by the red and yellow squares in (a), (b), (c) and (d). Some of dislocation loops studied are marked by arrows. Both 1/2<111> (red squares) and ⟨100⟩ (yellow squares) dislocation loops are observed. (For interpretation of the references to colour in this figure legend, the reader is referred to the web version of this article.)

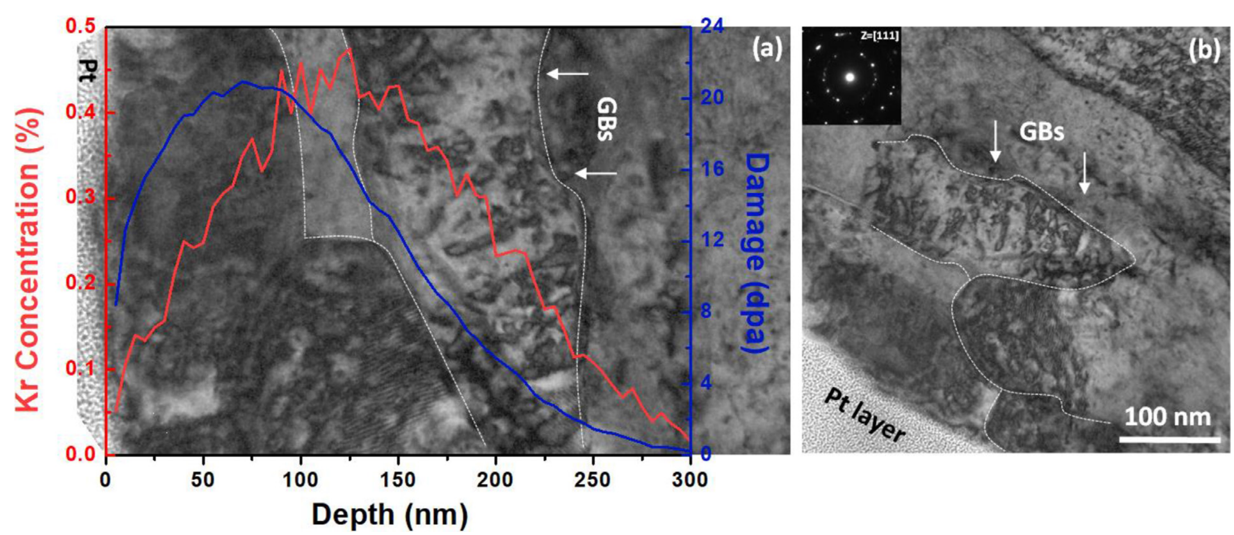

Fig. 6. (a) Sub-micron grains formed in Kr irradiated bulk tungsten. The top surface was protected by Pt layer and some of the GBs are marked by white arrows. (b) Highlight of the sub-micron grains formed after Kr irradiation. The misorienation angle is around 10° for these subgrains according to the diffraction pattern with Z=[111].

zero in the region beyond D = 1000 nm. However, irradiation defects, especially SIAs can migrate into deeper regime, as manifested by the formation of high density of dislocation loops at D = 1100 nm in Fig. 3f. The irradiation enhanced diffusion of SIAs was also reported in other metals [46–48].

Due to far less He concentration, radiation defects in thin-foil irradiation are significantly different from that of bulk He^+ implantation. As shown in Fig. 4f, cavities are formed in the He^+ irradiated thin-foil although the extreme low He concentration. Due to the sink effect of free surfaces, irradiation-induced SIAs migrate quickly from the center of the sample to top and bottom surfaces and annihilate, leading to the formation of profuse vacancy clusters in the interior of thin-foil sample [48–50]. The retained 0.1 at.% of He in TEM thin-foil still can trap a large number of vacancies. As a results, numerous He bubbles are formed in thin-foil irradiation as well. The volume fraction of cavities in both bulk (0.084%) and thin-foil tungsten (0.066%) were

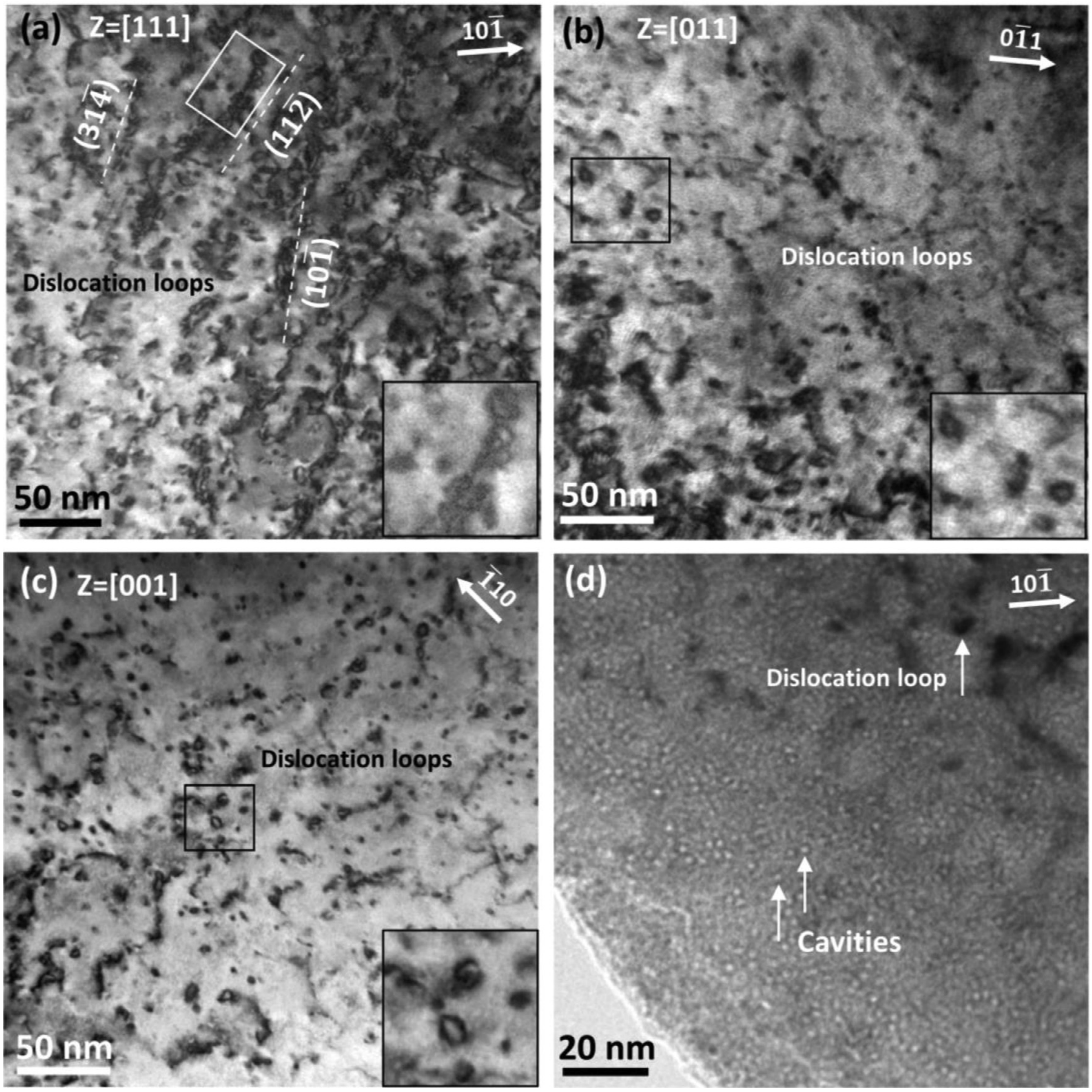

Fig. 7. Defects structures formed in Kr^+ irradiated TEM foil tungsten. Images of dislocation loops viewed with different orientation (a) *z*=[111], (b) *z*=[011] and (c) *z*=[001]. (d) High density of cavities formed in TEM foil tungsten.

measured and plotted in Fig. 8d. The volume fraction of cavities is determined by f=V_{He}N/V_{sample} where V_{He} is the average volume of one cavity, N is the number of cavities and V_{sample} is the volume of sample. The higher volume fraction of He bubbles in bulk tungsten is attributed to the higher He concentration and larger radiation damage. However, the volume fraction of cavities in TEM samples is only slightly less (~0.79 times) than that in the bulk sample, while the He concentration is only 1% and radiation damage is half of that in the bulk irradiation. Therefore, in TEM foils irradiation, the sink effect of surfaces lead to the quick annihilation of self-interstitials, which promote the accumulation of vacancies clusters, such as cavities. This is the likely reason why the volume fraction of cavities in thin-foil sample is comparable to the bulk He^+ implanted tungsten.

A large number of dislocation loop-aggregates appeared under viewing direction with *z*=[111] in TEM sample, as shown in Fig. 4. Loop strings were also developed in pure W under viewing directions of *z*=[001], [011] and [111], wherein a higher irradiation temperature (≥500 °C) and damage level are required for *z*=[001] after self-ions irradiation [22,23]. The 1D migration of 1/2 ⟨111⟩ interstitial loops with collinear geometry form the structure of loop strings and networks were observed, which was probably attributed to preferential loss of loop variants to surface in different grain orientations. The mechanism of loop rafting is considered due to loop glide and cluster-cluster interaction or cluster-dislocation interaction [51]. Nevertheless, our results demonstrate that the ordering of loops only appear with viewing direction of *z*=[111], and no obvious loop strings were observed in other orientations. Loops number densities of He implanted bulk and thin-foil tungsten are also compared in Fig. 8c, lower density of dislocation loops in bulk sample may be attributed to a large fraction of irradiation-induced SIAs evolved into low angle GBs.

4.2. Comparison of krypton irradiated bulk and thin-foil tungsten

The nature of irradiation defects is also investigated in detail in Kr^+ irradiated bulk and thin-foil tungsten. Similar to the He^+ irradiation, Kr^+ irradiated bulk tungsten has high density of sub-micron grains, as shown in Fig. 6. Much higher irradiation damage (~20 dpa) in Kr^+ implantation and irradiation-induced SIAs diffusion are responsible for the formation of sub-grain structures. Kr gas bubbles were reported in Kr^+ implanted tungsten at 525 K [52]. However, due to the low fluence in current experiments (~0.47 at.% Kr^+), no Kr gas bubbles were detected (see Fig. 6). Due to the relatively fast dpa rate under Kr^+ irradiation (0.02 dpa/s), the recombination of vacancies and SIAs are much higher than that in the He implantation, thus the

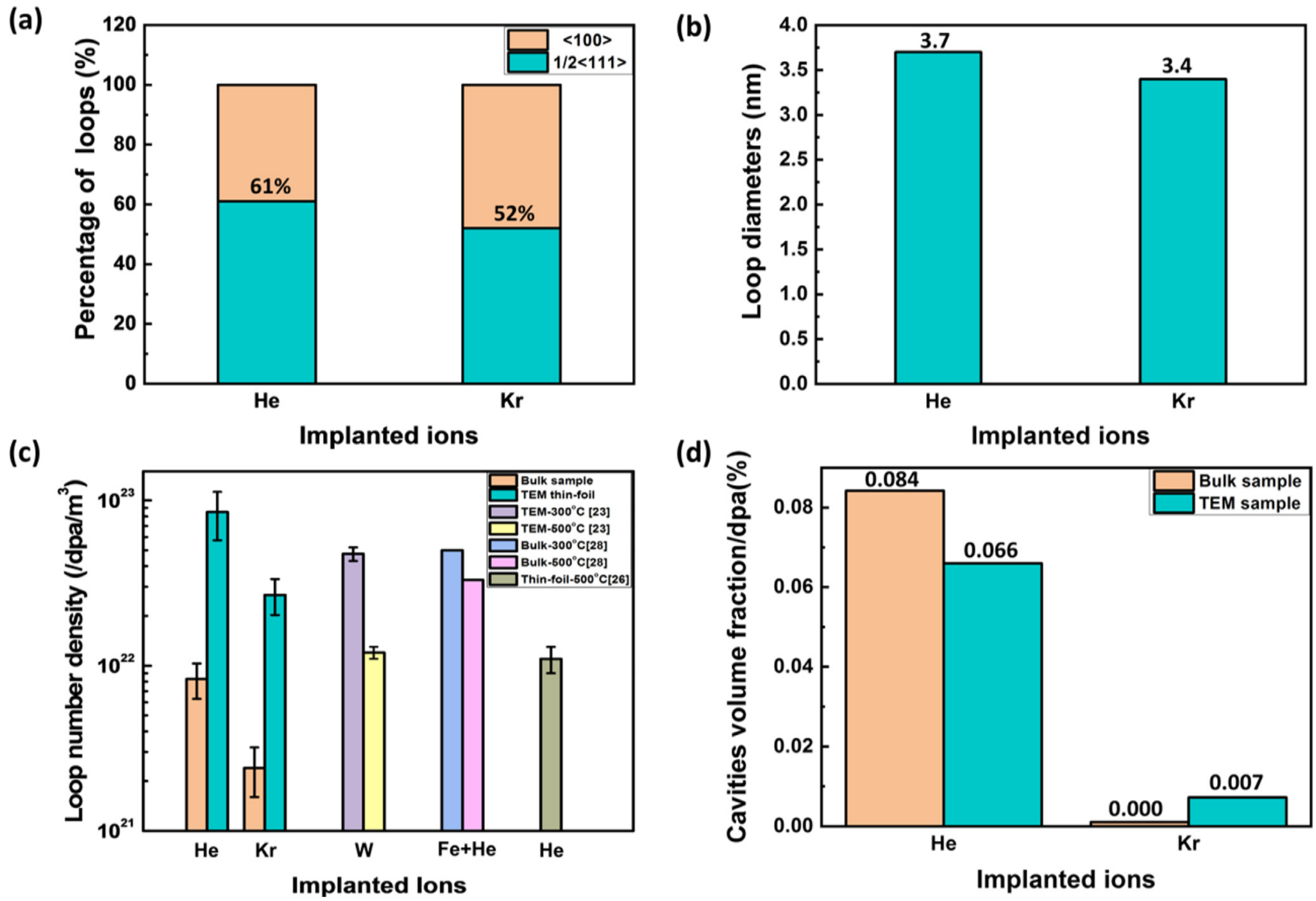

Fig. 8. Statistical plot showing the character of dislocation loops in He^+ and Kr^+ irradiated tungsten at 400 °C. (a) The percentage of 1/2<111> loops and ⟨100⟩ loops. (b) Average diameter of dislocations loop in He and Kr irradiated TEM foil tungsten. (c) Production rate of dislocation loops in irradiated bulk and thin-foil tungsten and compare with other studies [23,28,30]. (d) Volume fraction of cavities in He and Kr irradiated tungsten. The volume fraction of cavities in bulk sample was measured at the peak damaged region. The saturation damage for defect production under self-ion irradiation in tungsten is around 2.4 dpa according to [22,23], considering the atomic weight of Kr^+ is only half of W^+, thus the saturation damage under Kr^+ irradiation should be higher and assume to be 5 dpa in order to plot (c) and (d). For He^+ irradiation, the saturation damage should be much higher than 5 dpa, thus the defects accumulation is still in the linear accumulation stage for damage less than 3 dpa.

survived point defects are low. The diffusion of irradiation-induced SIAs plays a primary role for the defects recombination and sub-micron grains formation.

Cavities are detected in Kr^+ irradiated thin-foil tungsten, while no cavity were detected in Kr^+ implanted bulk tungsten, as shown in Fig. 6 and plotted in Fig. 8d. In thin-foil irradiation, due to the surface sink effect, a large fraction of SIAs were disappeared at the top and bottom surfaces, leaving high concentration of vacancies in the interior of sample, which is the origin of the cavities in Kr^+ thin-foil irradiation. On the contrary, the SIAs and vacancies have high recombination rate in Kr^+ implanted bulk tungsten, thus no cavities are observed. Dislocation loop clusters were also identified in Kr^+ implanted thin-foil sample, the formation mechanism of which is similar to the He implanted TEM tungsten (Fig. 7). The number density of dislocation loops is higher in Kr irradiated thin-foil samples than that in the bulk (Fig. 8c) because a large number of SIAs evolve into low angle GBs in Kr^+ bulk irradiation, thus fewer dislocation loops were produced.

4.3. Character of dislocation loops and cavities in irradiated tungsten

As shown in Fig. 8a and b, the fraction of 1/2<111> or ⟨100⟩ dislocation loops and their diameter were measured and plotted. The method to determine the fraction of dislocation loops with 1/2<111> or ⟨100⟩ Burgers vector is proposed by Yi et al. [22,23]. The Burgers vectors of dislocation loops were analyzed under g = 110, $\bar{1}10$, $\bar{2}00$ and 020 with invisibility criterion $g{\cdot}b = 0$. If the number of loops of any 1/2<111> variants appeared in the analyzed region is assigned x, and any ⟨100⟩ variant is set y, then the loop numbers in g = 110 and $\bar{1}10$ can be obtained by A=(4 x + 4 y), while loop numbers B=(8x + 2y) can be counted in g = $\bar{2}00$ and 020, respectively. A and B can be found by counting the total number of loops visible in each g vector. The fraction of 1/2<111> loops and ⟨100⟩ loops in the total population can be summarized as $4x/(4x+3y)$ and $3y/(4x+3y)$, respectively. Loop diameters are obtained by $D\sqrt{4A/\pi}$, where A is the loop areas. According to the measurement, the fraction of 1/2<111> loops are 61% and 52%, and the size of loops are 3.7 nm and 3.4 nm, for He^+ and Kr^+ irradiated TEM thin-foil, as displayed in Fig. 8a and b.

Only dislocation loops with Burgers vectors of 1/2<111> were reported in He implantation with energy of 15, 60 and 85 keV, while ⟨100⟩ loops were formed under 350 keV self-ion irradiation in tungsten [28,29,53]. The production of 1/2<111> is largely due to the clustering of SIAs, while the formation mechanisms of ⟨100⟩ loops is complex, and can be summarized as: direct dense cascade [54–57], Eyre–Bullough mechanism [58], interaction and reaction of two ⟨111⟩ loop variants [59,60] or spontaneous switch of Burgers vector through irradiation or heating [61]. W self-ion irradiation [54,62] produced various amount ⟨100⟩ loops (25% or 35–40%) due to collision cascade as result of the differing primary knock atom (PKA) energy. In general, the higher PKA energies will lead to a larger percentage of ⟨100⟩ loops due to the increased cascade size and density. Owing to the high atomic weight of heavy ions, a recoil deposits its energy in a fairly compact cascade, forming a concentrated area of high-energy density and increased thermal spike lifetime [55]. Similarly, the 400 keV He ions in this case could induce dense collision cascade damage in tungsten, which is much higher than other low He ion energy irradiation [28,29]. As a result, 39% of ⟨100⟩ loops were produced in He^+ irradiated tungsten. Even higher fraction of ⟨100⟩ loops (48%) were formed in Kr implanted thin-foil sample, which is also related to the higher PKA energy and compact collision cascade under heavy ion irradiation [63]. Our results also demonstrate that the formation of ⟨100⟩ loops is related to the PKA energy and the character of collision cascade [22,25,62].

As displayed in Fig. 8c and d, dislocation loops number density and the volume fraction of cavities are higher in He^+ irradiated thin-foil sample. Loop number densities per dpa under different zones are counted for He^+ and Kr^+ irradiated bulk and thin-foil tungsten, as calculated as $\rho=[n/(s \times t)]/\mathrm{dpa}_{sat}$, where n is the number of loops, s is the area of the region, t is the thickness of sample and dpa_{sat} is the saturation damage for defect production. According to Yi et al. [22,23], under self-ion irradiation, the radiation defects reached a saturation after 1.2 dpa at 300 °C, while reached a saturation after 3.6 dpa at 500 °C. According to this trend, the saturation damage should be around 2.4 dpa at 400 °C for self-ion irradiation. Based on the investigation on self-ion irradiation in tungsten, we estimate the saturation damage for Kr^+ irradiation is around 5 dpa at 400 °C (atomic weight of Kr^+ is half of W^+) and this value is adopted to calculate the loop number density in Fig. 8c. Defect character statistics from this work together with relevant researches [23,28,30] are summarized and plotted in Fig. 8c. As shown in Fig. 8c, loops number density in He^+ implanted tungsten is higher than that in Kr^+ implanted sample for both bulk and thin-foil samples. The loop number density is much higher in Fe^+ irradiated bulk tungsten with trace of He than that in Kr^+ irradiated sample. These phenomenon indicate that He can suppress the annihilation of defects and thus lead to the formation of higher density of dislocation loops [64]. In general, the loop number density is higher in thin-foil irradiation than that in bulk sample, which is related to high recombination rate of point defects in bulk irradiation, surface sink effect and long-range elastic fields which prevent the escape of loops from the foil [65]. For both He^+ and Kr^+ implantation, the visible loops number densities are highest in [111] orientation and lowest in [001] orientation.

The volume fraction of cavities in irradiated both thin-foil and bulk tungsten are plotted in Fig. 8d. Because of high binding energy of He-V, abundant He bubbles (0.084%) appear in bulk samples. Unlike the trapping of vacancies by He, the irradiation-induced SIAs can recombine efficiently with the vacancies in Kr^+ irradiation. Therefore, the survived total number of point defects per dpa is relatively low in Kr^+ irradiation than that in the He^+ implantation. Thus, fewer dislocation loops and no or lower volume fraction of cavities were produced in Kr^+ irradiated tungsten. In addition, high volume fraction of cavities are produced in thin-foil after He^+ implantation. Due to the 0.1 at.% of He concentration in thin-foil irradiation, vacancies can be trapped during implantation and evolved into cavities, while a high fraction of SIAs were disappeared at surfaces in thin-foil tungsten, the partially accumulated SIAs can form into dislocation loops. Although Kr^+ has a low binding energy with vacancies, due to the strong surface sink effect, the bias disappearing of SIAs at surfaces under thin-foil irradiation, small volume fraction of cavities can still form in Kr^+ irradiated thin-foil, which is totally different from the Kr^+ bulk implantation in Fig. 6. These results indicate that He^+ implantation can suppress irradiation defects recombination, promote the formation of more radiation defects, and is detrimental to the metals. The sink effects of surfaces have a marked influence on radiation defect dynamics during thin-foil irradiation, which should be pay attention in future investigations.

5. Conclusions

Radiation-induced defects within a wide range of dpa and ion concentration were investigated in He^+ or Kr^+ implanted both bulk and thin-foils tungsten. The sample surface sink effect, the recombination rate of radiation-induced point defects and the chemical and physical effect of implanted ions on the irradiation defect evolution and their formation mechanism were explored. Main findings are summarized as following:

1) Sub-micron grains were formed in the region close to the implanted surface in bulk tungsten due to diffusion and clustering of radiation-induced SIAs. The peak distribution of dislocation loop is formed beyond the maximum dpa and He concentration region. Dislocation loops were also identified in the region beyond the ion implanted regime. This phenomenon is also related to the irradiation-accelerated diffusion and clustering of SIAs during implantation.
2) Ordered dislocation loops are aligning along {110} and {112} planes under viewing direction of z=<111> in thin-foil irradiation. Both 1/2<111> and ⟨100⟩ dislocation loops were observed under both He^+ and Kr^+ irradiation. More ⟨100⟩ loops are detected in Kr^+ irradiation than that in He^+ implantation, which is attributed to the higher energy of collision cascade under heavy ion irradiation.
3) Radiation point defects recombination can be suppressed in He^+ implantation due to the strong binding energy of He with vacancies. As a result, the number of dislocation loop and the volume fraction of cavities are higher in He^+ implanted tungsten than that in the Kr^+ irradiation. Therefore, He^+ implantation can produce more radiation defects and induce severe damage than the Kr^+ irradiation under similar radiation conditions.
4) Due to the surface sink effect, cavities are formed in both He^+ and Kr^+ irradiated TEM foil tungsten. Recombination of interstitials and vacancies cannot be fully achieved because of the disappearing of SIAs at surface under thin-foil irradiation, in contrast to the efficient annihilation in Kr^+ irradiated bulk tungsten. Therefore, the effect of surface sinks on radiation defect dynamics need to be considered in future study.

Declaration of Competing Interest

The authors declare no competing financial interests.

Acknowledgements

This research was supported by the National Natural Science Foundation of China (Grant Nos. 51971170, 51922082 and 51942104), the National Key Research and Development Program of China (2017YFB0702301), the Innovation Project of Shaanxi Province (Grant No. 2017KTPT-12) and the 111 Project of China (Grant Number BP2018008).

References

[1] V. Philipps, Tungsten as material for plasma-facing components in fusion devices, J. Nucl. Mater. 415 (2011) S2–S9.
[2] S.J. Zinkle, L.L. Snead, Designing radiation resistance in materials for fusion energy, Annu. Rev. Mater. Res. 44 (2014) 241–267.
[3] J. Knaster, A. Moeslang, T. Muroga, Materials research for fusion, Nat. Phys. 12 (2016) 424–434.
[4] W. Jäger, M. Wilkens, Formation of vacancy-type dislocation loops in tungsten bombarded by 60keV au ions, Phys. Stat. Sol. (a) 32 (1975) 89–100.
[5] Q. Yang, H.Y. Fan, W.Y. Ni, L. Liu, T. Berthold, G. Benstetter, et al., Observation of interstitial loops in He^+ irradiated W by conductive atomic force microscopy, Acta Mater. 92 (2015) 178–188.
[6] H. Iwakiri, K. Yasunaga, K. Morishita, N. Yoshida, Microstructure evolution in tungsten during low-energy helium ion irradiation, J. Nucl. Mater. 283-287 (2000) 1134–1138.
[7] N. Yoshida, H. Iwakiri, K. Tokunaga, T. Baba, Impact of low energy helium irradiation on plasma facing metals, J. Nucl. Mater. 337–339 (2005) 946–950.

[8] O. El-Atwani, J.A. Hinks, G. Greaves, S. Gonderman, T. Qiu, M. Efe, et al., In situ TEM observation of the response of ultrafine- and nanocrystalline-grained tungsten to extreme irradiation environments, Sci. Rep. 4 (2014) 4716.
[9] F. Ferroni, X. Yi, K. Arakawa, S.P. Fitzgerald, P.D. Edmondson, S.G. Roberts, High temperature annealing of ion irradiated tungsten, Acta Mater. 90 (2015) 380–393.
[10] M. Toulemonde, C. Dufour, E. Paumier, Transient thermal process after a high-energy heavy-ion irradiation of amorphous metals and semiconductors, Phys. Rev. B 46 (1992) 14362–14369.
[11] X.X. Hu, T. Koyanagi, M. Fukuda, N.A.P. Kiran Kumar, L.L. Snead, B.D. Wirth, Y. Katoh, Irradiation hardening of pure tungsten exposed to neutron irradiation, J. Nucl. Mater. 480 (2016) 235–243.
[12] D.E.J. Armstrong, X. Yi, E.A. Marquis, S.G. Roberts, Hardening of self ion implanted tungsten and tungsten 5-wt% rhenium, J. Nucl. Mater. 432 (2013) 428–436.
[13] R. Causey, K. Wilson, T. Venhaus, W.R. Wampler, Tritium retention in tungsten exposed to intense fluxes of 100eV tritons, J. Nucl. Mater. 266−269 (1999) 467–471.
[14] T. Venhaus, R. Causey, R. Doerner, T. Abeln, Behavior of tungsten exposed to high fluences of low energy hydrogen isotopes, J. Nucl. Mater. 290-293 (2001) 505–508.
[15] A. Hasegawa, M. Fukuda, S. Nogami, K. Yabuuchi, Neutron irradiation effects on tungsten materials, Fusion Eng. Des. 89 (2014) 1568–1572.
[16] T. Tanno, A. Hasegawa, J.C. He, M. Fujiwara, M. Satou, S. Nogami, K. Abe, T. Shishidoet, Effects of transmutation elements on the microstructural evolution and electrical resistivity of neutron-irradiated tungsten, J. Nucl. Mater. 386-388 (2009) 218–221.
[17] A. Hasegawa, T. Tanno, S. Nogami, M. Satou, Property change mechanism in tungsten under neutron irradiation in various reactors, J. Nucl. Mater. 417 (2011) 491–494.
[18] M. Fukuda, A. Hasegawa, T. Tanno, S. Nogami, H. Kurishita, Property change of advanced tungsten alloys due to neutron irradiation, J. Nucl. Mater. 442 (2013) S273–S276.
[19] M. Fukuda, K. Yabuuchi, S. Nogami, A. Hasegawa, T. Tanaka, Microstructural development of tungsten and tungsten−rhenium alloys due to neutron irradiation in HFIR, J. Nucl. Mater. 455 (2014) 460–463.
[20] M. Klimenkov, U. Jäntsch, M. Rieth, H.C. Schneider, D.E.J. Armstrong, J. Gibson, et al., Effect of neutron irradiation on the microstructure of tungsten, Nucl. Mater. Energ. 9 (2016) 480–483.
[21] S.J. Zinkle, K. Farrell, Void swelling and defect cluster formation in reactor-irradiated copper, J. Nucl. Mater. 168 (1989) 262–267.
[22] X. Yi, M.L. Jenkins, M.A. Kirk, Z.F. Zhou, S.G. Roberts, In-situ TEM studies of 150keV W^{+} ion irradiated W and W-alloys: damage production and microstructural evolution, Acta Mater. 112 (2016) 105–120.
[23] X. Yi, M.L. Jenkins, K. Hattar, P.D. Edmondson, S.G. Roberts, Characterisation of radiation damage in W and W-based alloys from 2 MeV self-ion near-bulk implantations, Acta Mater. 92 (2015) 163–177.
[24] J. Grzonka, Ł. Ciupiński, J. Smalc-Koziorowska, O.V. Ogorodnikova, M. Mayer, K.J. Kurzydłowski, Electron microscopy observations of radiation damage in irradiated and annealed tungsten, Nucl. Instrum. Methods Phys. Res. B 340 (2014) 27–33.
[25] O. El-Atwani, E. Esquivel, M. Efe, E. Aydogan, Y.Q. Wang, E. Martinez, et al., Loop and void damage during heavy ion irradiation on nanocrystalline and coarse grained tungsten: microstructure, effect of dpa rate, temperature, and grain size, Acta Mater. 149 (2018) 206–219.
[26] O. El-Atwani, K. Hattar, J.A. Hinks, G. Greaves, S.S. Harilal, A. Hassanein, Helium bubble formation in ultrafine and nanocrystalline tungsten under different extreme conditions, J. Nucl. Mater. 458 (2015) 216–223.
[27] O. El-Atwani, E. Esquivel, E. Aydogan, E. Martinez, J.K. Baldwin, M. Li, et al., Unprecedented irradiation resistance of nanocrystalline tungsten with equiaxed nanocrystalline grains to dislocation loop accumulation, Acta Mater. 165 (2019) 118–128.
[28] R.W. Harrison, G. Greaves, J.A. Hinks, S.E. Donnelly, A study of the effect of helium concentration and displacement damage on the microstructure of helium ion irradiated tungsten, J. Nucl. Mater. 495 (2017) 492–503.
[29] R.W. Harrison, H. Amari, G. Greaves, J.A. Hinks, S.E. Donnelly, Effect of HE-APPM/DPA ratio on the damage microstructure of tungsten, MRS Adv. 1 (2016) 2893–2899.
[30] Z.X. Zhang, K. Yabuuchi, A. Kimura, Defect distribution in ion-irradiated pure tungsten at different temperatures, J. Nucl. Mater. 480 (2016) 207–215.
[31] I. Ipatova, R.W. Harrison, D. Terentyev, S.E. Donnelly, E. Jimenez-Melero, Thermal evolution of the proton irradiated structure in tungsten−5 wt% tantalum, J. Fusion Energy 36 (2017) 234–239.
[32] R.W. Harrison, N. Peng, R.P. Webb, J.A. Hinks, S.E. Donnelly, Characterisation of helium ion irradiated bulk tungsten: a comparison with the in-situ TEM technique, Fusion Eng. Des. 138 (2019) 210–216.
[33] J.F. Ziegler, M.D. Ziegler, J.P. Biersack, SRIM − the stopping and range of ions in matter, Nucl. Instrum. Methods Phys. Res. B 268 (2010) 1818–1823.
[34] Q. Xu, T. Yoshiie, H.C. Huang, Molecular dynamics simulation of vacancy diffusion in tungsten induced by irradiation, Nucl. Instrum. Methods Phys. Res. B 206 (2003) 123–126.
[35] R.E. Stoller, M.B. Toloczko, G.S. Was, A.G. Certain, S. Dwaraknath, F.A. Garner, On the use of SRIM for computing radiation damage exposure, Nucl. Instrum. Methods Phys. Res. B 310 (2013) 75–80.
[36] S. Agarwal, A. Bhattacharya, P. Trocellier, S.J. Zinkle, Helium induced microstructure damage, nano-scale grain formation and helium retention behaviour of ZrC, Acta Mater. 163 (2019) 14–27.
[37] P.J. Yang, W.Z. Han, Enhanced oxidation resistance in refractory niobium by surface Ti+/Si+ implantation, Corros. Sci. (2019), doi: 10.1016/j.corsci.2019.108297.
[38] W.Z. Han, Z.F. Zhang, S.D. Wu, S.X. Li, Influences of crystallographic orientations on deformation mechanism and grain refinement of Al single crystals subjected to one-pass equal-channel angular pressing, Acta Mater. 55 (2007) 5889–5900.
[39] W.Z. Han, H.J. Yang, X.H. An, R.Q. Yang, S.X. Li, S.D. Wu, et al., Evolution of initial grain boundaries and shear bands in Cu bicrystals during one-pass equal-channel angular pressing, Acta Mater. 57 (2009) 1132–1146.
[40] S.H. Li, J. Z, W.Z. Han, Helium bubbles enhance strength and ductility in small-volume Al-4Cu alloys, Scr. Mater. 165 (2019) 112–116.
[41] D.E. Rimmer, A.H. Cottrell, The solution of inert gas atoms in metals, Philos. Mag. 2 (1957) 1345–1353.
[42] T. Seletskaia, Y.N. Osetsky, R.E. Stoller, G.M. Stocks, Calculation of helium defect clustering properties in iron using a multi-scale approach, J. Nucl. Mater. 351 (2006) 109–118.
[43] F. Gao, H.Q. Deng, H.L. Heinisch, R.J. Kurtz, A new Fe−He interatomic potential based on ab initio calculations in α-Fe, J. Nucl. Mater. 418 (2011) 115–120.
[44] P.H. Chen, X.C. Lai, K.Z. Liu, X.L. Wang, B. Bai, B.Y. Ao, et al., Development of a pair potential for Fe−He by lattice inversion, J. Nucl. Mater. 405 (2010) 156–159.
[45] S.H. Li, J.T. Li, W.Z. Han, Radiation-induced helium bubbles in metals, Materials 12 (2019) 1036.
[46] R. Sizmann, The effect of radiation upon diffusion in metals, J. Nucl. Mater. 69−70 (1978) 386–412.
[47] V. Naundorf, Diffusion in metals and alloys under irradiation, Int. J. Mod. Phys. B 18 (1992) 2925–2986.
[48] M. Wang, I.J. Beyerlein, J. Zhang, W.Z. Han, Defect-interface interactions in irradiated Cu/Ag nanocomposites, Acta Mater. 160 (2018) 211–223.
[49] M. Wang, I.J. Beyerlein, J. Zhang, W.Z. Han, Bi-metal interface-mediated defects distribution in neon ion bombarded Cu/Ag nanocomposites, Scr. Mater. 171 (2019) 1–5.
[50] W.Z. Han, M.J. Demkowicz, N.A. Mara, E.G. Fu, S. Sinha, A.D. Rollett, et al., Design of radiation tolerant materials via interface engineering, Adv. Mater. 25 (2013) 6975–6979.
[51] O. El-Atwani, E. Aydogan, E. Esquivel, M. Efe, Y.Q. Wang, S.A. Maloy, Detailed transmission electron microscopy study on the mechanism of dislocation loop rafting in tungsten, Acta Mater. 147 (2018) 277–283.
[52] G. Ran, S.L. Huang, Z.J. Huang, Q.Z. Yan, J.K. Xu, N. Li, et al., In situ observation of microstructure evolution in tungsten under 400keV Kr+ irradiation, J. Nucl. Mater. 455 (2014) 320–324.
[53] R.W. Harrison, J.A. Hinks, S.E. Donnelly, Influence of pre-implanted helium on dislocation loop type in tungsten under self-ion irradiation, Scr. Mater. 150 (2018) 61–65.
[54] A.F. Calder, D.J. Bacon, A.V. Barashev, Y.N. Osetsky, Effect of mass of the primary knock-on atom on displacement cascade debris in α-iron, Philos. Mag. Lett. 88 (2008) 43–53.
[55] A.E. Sand, S.L. Dudarev, K. Nordlund, High-energy collision cascades in tungsten: dislocation loops structure and clustering scaling laws, EPL 103 (2013) 46003.
[56] A.E. Sand, K. Nordlund, S.L. Dudarev, Radiation damage production in massive cascades initiated by fusion neutrons in tungsten, J. Nucl. Mater. 455 (2014) 207–211.
[57] W. Setyawan, G. Nandipati, K.J. Roche, H.L. Heinisch, B.D. Wirth, R.J. Kurtz, Displacement cascades and defects annealing in tungsten, part I: defect database from molecular dynamics simulations, J. Nucl. Mater. 462 (2015) 329–337.
[58] B.L. Eyre, R. Bullough, On the formation of interstitial loops in B.C.C. metals, Philos. Mag. 12 (1965) 31–39.
[59] A.E. Ward, S.B. Fisher, Dislocation loop growth in pure iron under electron irradiation, J. Nucl. Mater. 166 (1989) 227–234.
[60] J. Marian, B.D. Wirth, J.M. Perlado, Mechanism of formation and growth of <100> interstitial loops in ferritic materials, Phys. Rev. Lett. 88 (2002) 255507.
[61] K. Arakawa, M. Hatanaka, E. Kuramoto, K. Ono, H. Mori, Changes in the burgers vector of perfect dislocation loops without contact with the external dislocations, Phys. Rev. Lett. 96 (2006) 125506.
[62] X. Yi, M.L. Jenkins, M. Briceno, S.G. Roberts, Z. Zhou, M.A. Kirk, In situ study of self-ion irradiation damage in W and W−5Re at 500°C, Philos. Mag. 93 (2013) 1715–1738.
[63] S.J. Zinkle, B.N. Singh, Analysis of displacement damage and defect production under cascade damage conditions, J. Nucl. Mater. 199 (1993) 173–191.
[64] F.F. Luo, Z. Yao, L.P. Guo, J.P. Suo, Y.M. Wen, Convoluted dislocation loops induced by helium irradiation in reduced-activation martensitic steel and their impact on mechanical properties, Mater. Sci. Eng. A 607 (2014) 390–396.
[65] D.R. Mason, X. Yi, M.A. Kirk, S.L. Dudarev, Elastic trapping of dislocation loops in cascades in ion-irradiated tungsten foils, J. Phys. Condens. Matter 26 (2014) 375701.